Journal of Inorganic and Organometallic Polymers and Materials (2024) 34:759–772
https://doi.org/10.1007/s10904-023-02802-w

RESEARCH

Facile Construction of Novel Ag/Er_2O_3@CuO Nanocomposite for Superior Visible-light-driven Photocatalytic Degradation and Antibacterial Activity

M. Arunpandian[1] · L.T. Parvathi[2] · K. Selvakumar[1] · Tae Hwan Oh[1] · S. Karuthapandian[3]

Received: 1 June 2023 / Accepted: 13 July 2023 / Published online: 21 September 2023

Abstract
In this study, a novel Ag/Er_2O_3@CuO nanocomposite was synthesized by a simple hydrothermal method to evaluate both its efficiency for visible light-driven degradation of Amaranth (AM) dye, as well as its biological performance against various microorganisms such as *Vibrio culture, Serratia marcescens, Hemophilus influenzae*, and *Aeromonas hydrophila.* The physicochemical properties of the Ag/Er_2O_3@CuO nanocomposite were determined by UV-Vis spectroscopy, X-ray diffraction (XRD), Scanning electron microscopy (SEM), Energy-dispersive X-ray (EDX) spectroscopy, and X-ray photoelectron spectroscopy. The XRD results indicated the peak intensities of the Ag/Er_2O_3@CuO nanocomposite. The SEM images highlighted the morphology of the samples, revealing clearly structured spherically-shaped Ag elements that were well dispersed in the Er_2O_3/CuO composite matrix. XPS analysis revealed the elemental composition of the as-prepared nanocomposites. The greater zones of inhibition between the activities of each nanocomposite were indicative of their enhanced sensitivity for the abovementioned bacteria. Compared with the other regions, the Ag/Er_2O_3@CuO zones performed exceptionally well. Within 30 min, the AM dye was completely mineralized via photocatalytic degradation. The Ag/Er_2O_3@CuO nanocomposite's antibacterial efficacy against *Hemophilus influenzae* and *Aeromonas hydrophilia* was attributed to its wide surface area, increased reactivity due to its reduced size, and augmented formation of reactive oxygen species (ROS). During the photocatalytic degradation process, the AM dye was completely mineralized within 30 min. The optical parameters are also explained.

Keywords Antibacterial activity · Ag/Er_2O_3@CuO · Organic pollutants · Visible light · Disk diffusion · Amaranth

1 Introduction

Owing to the complex hierarchical structure and susceptibility of human tissue to damage from trauma, cancer, and other degenerative disorders [1], developing new ways of regenerating and managing injured human tissue is crucial. Refined biomaterials and tissue-engineered scaffolds are two common types of materials used for this purpose; however, they pose a higher risk of bacterial infection, that is associated with the insertion of foreign equipment or materials into the human body [2]. In sterile environments, such as operating rooms, even a single bacterium can cause an infection that can prove fatal. Implant failure and patient suffering can result from bacterial infections that may occur months to years after surgery [3]. In view of this, in this study we focus primarily on the processes and antibacterial capabilities of various metal ions and metal nanoparticles utilized in the development of biomaterials and structures, with the potential to reduce the severity of harmful bacterial infections. Infectious diseases caused by bacteria pose major health and financial concerns. For instance, the treatment of implant-associated osteomyelitis was projected to

M. Arunpandian and L.T. Parvathi contributed equally to this work.

✉ Tae Hwan Oh
taehwanoh@ynu.ac.kr

[1] School of Chemical Engineering, Yeungnam University, Gyeongsan 38541, Republic of Korea

[2] Sri Kaliswari College, Sivakasi, Tamilnadu 626123, India

[3] Department of Chemistry, V. H. N. Senthikumara Nadar College (Autonomous), Virudhunagar, Tamilnadu 626001, India

have cost more than $1.62 billion in the United States by 2020 [4]. A growing body of research aims to combat the steady spread of bacterial resistance by creating new antimicrobials. Bacterial cell-wall formation, DNA replication, and the protein translation machinery are the primary targets of antibiotics. However, the versatile resistance mechanisms of bacteria to antibiotics remain a concern. Efflux pumps, changes in cell morphology, amino acid substitutions, and post-translational modifications are examples of resistance mechanisms [5]. The production of enzymes that degrade, modify, or inactivate corresponding antibiotics (such as -lactamases) is another example. Antibacterial materials that work effectively and last for a long time are urgently required because of the growing threat posed by bacteria that are resistant to antibiotics. Much research has been conducted on the antibacterial qualities of metals that have been in use for centuries. Several metals are required for the biochemistry and metabolism of all living things, it is crucial to note that several metals are required for cellular activity [6, 7]. Copper, manganese, iron, and zinc are examples of essential metal ions (M^{n+}) that play crucial roles in the formation of cell membranes and DNA, as well as in fundamental cellular activities such as electron transfer and catalysis [8, 9]. Extremely high concentrations of essential metals such as iron and copper can be toxic to cells [10].

The non-essential metals silver (Ag) and mercury (Hg), on the other hand, are toxic even in trace amounts. In the same way that bacteria and mammals have different transport systems and metalloproteinase, metals have different effects on these two types of organisms [11]. This paves the way for the use of metal-based nanoparticles in long-term antibacterial therapy with minimal or no host side effects. Extensive research has been conducted on metal ions and the development of metal nanoparticles (M-NPs) with potent antibacterial activities [12–15]. Potential exists for M^{n+} and M-NPs significantly reduced or eradicated antibiotic-resistant microorganisms. The breakdown of DNA and proteins, two of the most crucial cellular components, has been reported as a mechanism of action [16–19]. Silver (Ag), Gold (Au), Copper (Cu), Zinc (Zn), and their oxides are frequently utilized.

Because of their high price and complexity, many detection methods currently employed are ineffective. The need for a cheap, dependable device that can accurately and reliably detect organic pollutants without interference has never increased. Scientists are inspired to create semiconductor nanostructure materials because of their superior mechanical strength, heat resistance, electro catalytic qualities, electrical conductance/properties, electromagnetic properties, and electro-catalytic and photo-catalytic capabilities [20, 21]. Recent studies have shown that the improved physicochemical properties of Nano-structured doped metal oxides are a major factor in their increasing popularity. The physicochemical properties of the doped metal oxide were improved by doping with semiconductor metal ions at varying concentrations, and these qualities were modified as needed [22–28].

In this regard, metal oxides based on the lanthanide sequence are considered an essential resource in the materials research field and are increasingly used in catalytic activity, absorption, and battery storage applications, owing to their unique semiconducting and paramagnetic properties, high-temperature stability, and fluorescent properties [29–31]. Erbium oxide (Er_2O_3) is a lanthanide that has greatly attracted the interest of chemists and physicists owing to its superior semiconductivity, specific heat capacity, and reduced toxicity, that render it an ideal catalyst for a variety of applications, from batteries and sensors, to biosensors and photocatalysis processes [32–34]. When introduced as a dopant in semiconductor catalysts for photosynthesis, it improves their light absorption performance and photogenerated electron production. In addition, it can boost the naturally lower intensity of infrared photons. The up-conversion mechanism described above can successfully improve the overall photocatalytic efficacy of semiconductor catalysts [35, 36]. Doping with semiconductor transition metals can improve the electrical conductivity of rare earth elements [37]. These doped nanomaterials have the added benefit of acting as electron mediators in tailor-made electrodes for the ultrasensitive detection of a wide variety of dangerous compounds using electrochemical and photocatalytic techniques.

Erbium was combined with copper in this method to develop altered semiconductor nanostructure components with enhanced electrical and photocatalytic performances. This is because CuO has the best electrical properties among semiconductor transition metal oxide [38]. Due to their useful physical and chemical properties [39], CuO NPs have several potential applications. There are only a few examples of thermoelectric [40], antioxidant [41], antibacterial [42], catalytic [43], solar cell [44], battery [45], Toxic Gas Detection [46–48], and chemical and biomolecular Compound Detection [49, 50] applications. It has been shown that the physical and chemical properties of CuO nanoparticles can be drastically changed by doping or mixing them with other nanomaterials [21, 49–51]. Multiple methods have been reported for producing copper (II)oxide nanoparticles (CuO-NPs) [52, 53], including sonochemical, wet chemical, direct thermal decomposition, microwave, solution plasma, pulsed wire explosion, and sol-gel methods. Researchers have also focused on photocatalytic degradation and other environmentally friendly cleaning practices a lot of attention. As a thriving branch of complex oxidation processes, photocatalysis has proven to be one of the

most efficient methods for the complete mineralization of toxic organic contaminants [54–56]. Further evidence of its efficacy and economic viability [57–61] is that reactive oxygen species (ROS) can be created with affordable resources, such as semiconductor materials, water, and light photons.

However, agglomeration and recombination phenomena can severely hinder the photocatalytic performance of the host Er_2O_3 material. In this regard, doping with CuO and Ag elements to create heterojunctions, and employing metal oxides to reduce aggregation, have been proven as viable methods to solve this issue. In view of this, in this work, we developed Ag-doped Er_2O_3/CuO nanomaterial composites that satisfy the criteria of low cost, high efficiency, light weight, and eco-friendly performance, for antimicrobial and environmental applications. The antibacterial action of our developed nanomaterials against a variety of different microorganisms, i.e., *Vibrio culture, Serratia marcescens, Hemophilus influenza, and Aeromonas*, was evaluated using a disc-and-well diffusion method. Further, their photocatalytic degradation efficacy against an AM dye effluent was investigated, reaching an exceptional 98.3% degradation rate within 30 min. This performance notably surpasses those of Er_2O_3 and CuO in previous reports. To the best of our knowledge, this is the first publication regarding the photocatalytic degradation efficiency and antimicrobial activity of Ag/Er_2O_3@CuO nanomaterials, thus offering valuable insights to fellow researchers in this field.

2 Experimental Section

2.1 Materials

The Ag/Er_2O_3/CuO nanocomposite was synthesized via hydrothermal process using Copper chloride (> 99.99%), Erbium nitrate hexahydrate (> 99.9%), Silver nitrate (> 99.0%), Urea (> 99.0%), Sodium hydroxide (> 98%), Ethanol (> 99.8%), and deionized water as reacting precursors (all obtained from Merck Chemicals, India and Sri Ganapathy Scientific Chemicals, Srivilliputhur, Tamilnadu, India).

2.2 Synthesis of CuO Nanoparticles

The CuO nanoparticles were generated using a hydrothermal method. The 20 mL of 0.1 M $CuCl_2$ were dissolved in water (20 mL) using a magnetic stirrer. The solution was magnetically stirrer for an hour as 10 mL of 1 M NaOH was slowly added. The prepared samples were washed extensively with distilled water before being placed in an autoclave and heated to 150 °C for 6 h. For the purpose of obtaining the CuO NPs, the material was first dried in an oven at 70 °C for 4 h before being calcined at 500 °C.

2.3 Synthesis of Er_2O_3 Particles

A reaction mixture containing 10 mL of 0.01 M Erbium (III) nitrate solution, 100 mL of water, and 0.5 mL of ammonia was transferred to an autoclave and subjected to hydrothermal treatment at 160 °C for 12 h. The precipitates formed from the hydrothermal reaction were thoroughly washed with deionized water and ethanol and then dried in an electric oven at 70 °C for 24 h. The Er_2O_3 nanomaterial was made by subjecting the as-synthesized samples to thermal treatment at 550 °C for 4 h in an electrical furnace with air circulation.

2.4 Synthesis of Ag/Er_2O_3@CuO Composites

The two suspensions were simultaneously mixed and stirred for ½ hr. A silver nitrate solution was added dropwise to the mixture. After the hydrothermal treatment, the as-prepared materials Ag/Er_2O_3@CuO were washed with water and dried in an oven at 70 °C for 5 h. In conclusion, the dried sample of Ag/Er_2O_3@CuO was taken exactly as it had been prepared and calcined at 550 °C. Figure 1 shows the synthesis of the Ag/Er_2O_3@CuO nanocomposites.

2.5 Degradation Performance Analysis

When the polluted sample was subjected to the as-synthesized Ag/Er_2O_3@CuO, it was destroyed by increased solar radiation. Approximately 30 mg/L of the photocatalyst were dispersed in 0.1 L (10 ppm) amaranth dye (AM) (10 mg/L) solution under dark conditions for 30 min, until the adsorption-desorption equilibrium was reached. The degradation process began after the dispersed mixture was added to the reaction tank and the tungsten lamp source was turned on (150 W). To measure the pollutant concentration, it was necessary to take samples of the degradation process at regular intervals and analyze them using a UV-Vis spectrophotometer (UV-2600, SHIMADZU, Japan). After centrifuging the suspension at 8500 rpm for 10 min to remove all nanoparticles, the catalyst was subjected to a continuous recycling radiation technique to assess the effectiveness of degradation and, by extension, the viability for future reuse.

$$Photodegradation\ efficiency = \left(1 - \frac{c}{c_0}\right) \times 100\% \quad (1)$$

where the initial concentration is denoted by C_0 and the dye concentration at that time is given by C.

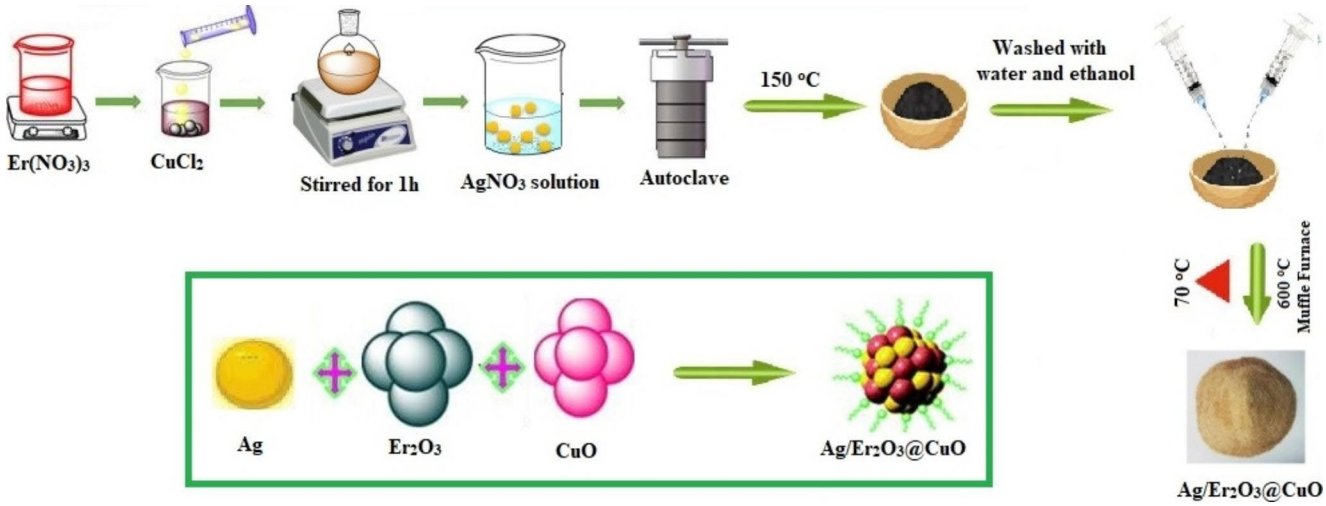

Fig. 1 Graphical representation of synthesize of $Ag/Er_2O_3@CuO$ nanocomposite

2.6 Antibacterial Performance Tests

Microorganisms such as *Vibrio culture, Serratia marcescens, Hemophilus influenza* and *Aeromonas* were tested using the Er_2O_3, CuO, and $Ag/Er_2O_3@CuO$ nanocomposites. The antibacterial efficacy was evaluated using Kirby-Bauer disc diffusion and microdilution with optical density techniques. All testing materials for antibacterial treatments were sterilized by heating to 120 °C for 15 min. A laminar flow cabinet was used for all microbiological applications.

2.6.1 Disk Diffusion Method

Individual bacterial cells were cultured in Mueller-Hinton broth for 24 h. A Mueller-Hinton agar plate was prepared in a glass Petri dish, and 100 L of bacterial culture, totaling approximately 6 × 107 CFU, was streaked evenly across the surface. About 6-mm diameter paper discs were impregnated with 25, 50, and 75% CuO, Er_2O_3, and $Ag/Er_2O_3@CuO$. Separate discs of impregnated paper were carefully placed on agar plates that had been streaked with different microorganisms. The agar plates were kept at 37 °C for 12 h. To evaluate the antibacterial properties of the nanocomposites, we observed and documented the size of any visible zones of inhibition around the periphery of the paper discs after they had been impregnated with the solution.

2.7 Characterization of $Ag/Er_2O_3@CuO$ Composites

The phase purity of the as-prepared materials was examined using a Philips X' PERTPRO powder X-ray diffractometer with a step size of 0.02°. The resulting sample micrographs and elemental compositions were studied using a scanning electron microscope calibrated using a model (SEM ZEISS – Sigma 300 microscope). The particle size was calculated from various digitized SEM images using the ImageJ software. The band energy of each synthesized sample was determined using a UV-visible spectrometer (Shimadzu UV-2600). Surface chemical analysis of the samples was conducted via X-ray photoelectron spectroscopy (XPS) using the ESCA-3 model. A Shimadzu UV-1800 UV-visible spectrophotometer was used to study the absorption wavelengths of the degraded organic pollutant samples.

3 Results and Discussion

3.1 Structural Analysis

The Ag, Er_2O_3, CuO, and $Ag/Er_2O_3@CuO$ nanocomposites exhibit distinct P-XRD patterns, as shown in Fig. 2. Powder diffraction analysis following Joint Committee standards was used to determine the phase purity of the as-prepared nanomaterials. The possible locations of 2θ peak intensity are (110), (111), (112), (020), (202), (-113), (-311), (220) and (311), respectively. All observed peaks are in good agreement with the JCPDS file (No. 45–0937) [62]. Diffraction planes at (222), (400), (440), and (622) are also observed in the spectra, indicating the presence of Er_2O_3 in addition to CuO in the produced nanomaterial (JCPDS-77-0459) [63]. The four peaks at 38.79°, 44.12°, 64.92°, and 78.09° corresponded well with the (111), (200), (220), and (311) planes of Ag [64]. Figure 2 shows the elongated diffraction peaks in the (222) plane of the Er_2O_3 and $Ag/Er_2O_3@CuO$ nanocomposite materials. A comparison of the peak intensities revealed that the $Ag/Er_2O_3@CuO$ nanocomposite significantly outperformed Er_2O_3.

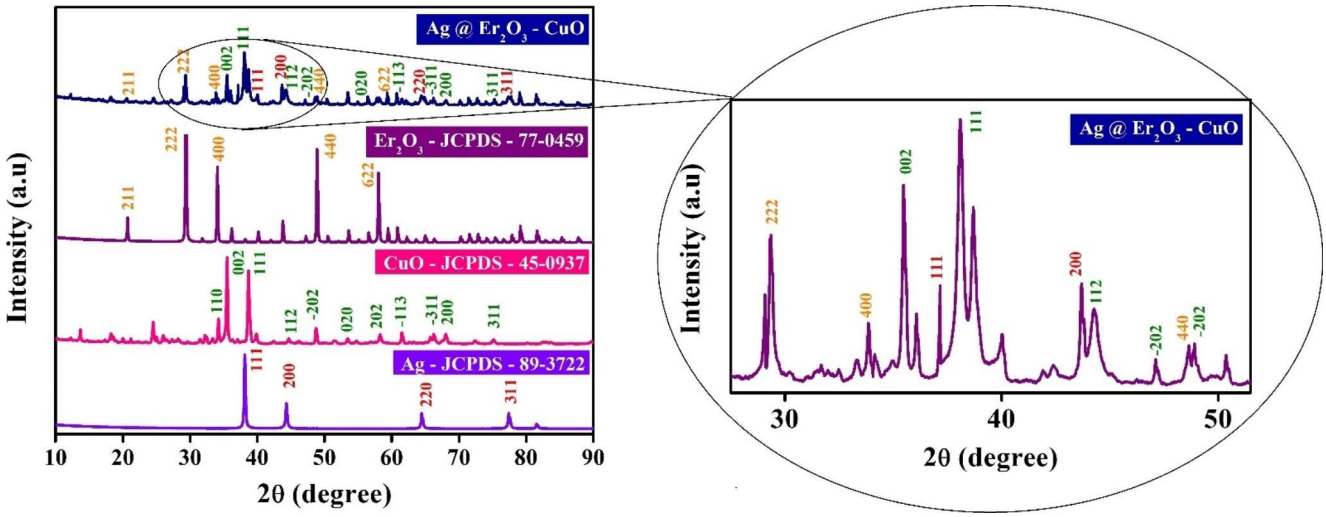

Fig. 2 Observed P-XRD profile of Ag, Er_2O_3, CuO, and Ag/Er_2O_3@CuO nanocomposite

3.2 Morphology Analysis

The SEM-EDS and elemental color mapping images of the Ag/Er_2O_3@CuO nanocomposites (Fig. 3) revealed the presence of Ag, Er, O, and Cu. The EDAX spectra (Fig. 3i, j, k) revealed the presence of Ag, Er, O, and Cu in the host and coupled nanocomposites. Also, as depicted in Fig. 3g, h, spherical Ag species were well deposited on the surface of the Er_2O_3@CuO hybrids. The surfaces of the nanorods were mostly covered with Ag spheres, and it was difficult to detect isolated Ag nanoparticles. The Er_2O_3@CuO composites were almost completely encased in Ag nanoparticles, while the host Er_2O_3 materials were well dispersed with CuO. The total weight percentages of each component of the as-prepared nanocomposite are illustrated in Table S1.

3.3 XPS Analysis

The elemental makeup, host state, and dopant components of the nanocomposites were investigated using X-ray photoelectron spectroscopy. The presence of Ag, Er, Cu, and O in Fig. 4 (b)–(f) proves that the Ag/Er_2O_3@CuO nanocomposites were indeed synthesized. The XPS spectra of Er 4d, Ag 3d, Cu 2p, and O 1s are shown in Fig. 4 (c-f). The binding energies of the electronic states of Cu $2p_{3/2}$ (933.1 eV) and Cu$2p_{1/2}$ (952.9 eV) [65] are shown in Fig. 4 (e). As a result of the erbium ions being in the +3-oxidation state in the host lattice, the Er 4d spectrum displays a peak with a center energy of 169.2 eV. The absorbed oxygen species are located at the 530.8 eV peak in O 1s, while the 530.1 eV and 533.1 eV peaks, which are associated with de-convolution, pertain to the lattice and chemical oxygen, respectively [66]. The $3d_{3/2}$ Ag(I) has a central feature peak at 376.5 eV, and the $3d_{5/2}$ Ag(I) provides strong evidence for silver's oxidation state with a peak at 370.6 eV [67, 68]. The synthesis of the nanomaterial confirmed the presence of Ag/Er_2O_3@CuO, as shown by the results.

3.4 Photoluminescence Analysis (PL)

PL analysis is an effective method for examining the quality, purity, and optical properties of materials. The remarkable light-absorbing properties of our developed nanocomposites render them promising candidates for various applications. The three emission peaks at 396, 426, and 465 nm in the PL visible emission spectra of the produced CuO and Ag/Er_2O_3@CuO nanomaterials at an excitation wavelength of 225 nm (Fig. S1) corresponded to violet, blue, and green emissions, respectively. The transition vacancies of oxygen and interstitial oxygen were responsible for the violet and blue emission bands, respectively, while single-ionized oxygen causes the emission band to be visible as green light. Overall, our nanomaterial exhibited prominent visible-range emission bands. According to these findings, the photocatalytic activity of the CuO nanoparticles was reduced owing to the elevated recombination rate of photoinduced charge carriers, as also indicated by the strong PL intensity. The photocatalytic performance of the CuO nanomaterials was improved by introducing Ag and Er_2O_3 nanoparticles on their surfaces, which significantly inhibited charge-carrier recombination. The PL intensity and photocatalytic activity in this study were strongly correlated.

3.5 BET Analysis

The surface area and pore volume of the Ag/Er_2O_3@CuO nanocomposites were calculated using the Brunauer-Emmett-Teller (BET) method as 142.49 m^2/g and 0.089 cm^3/g,

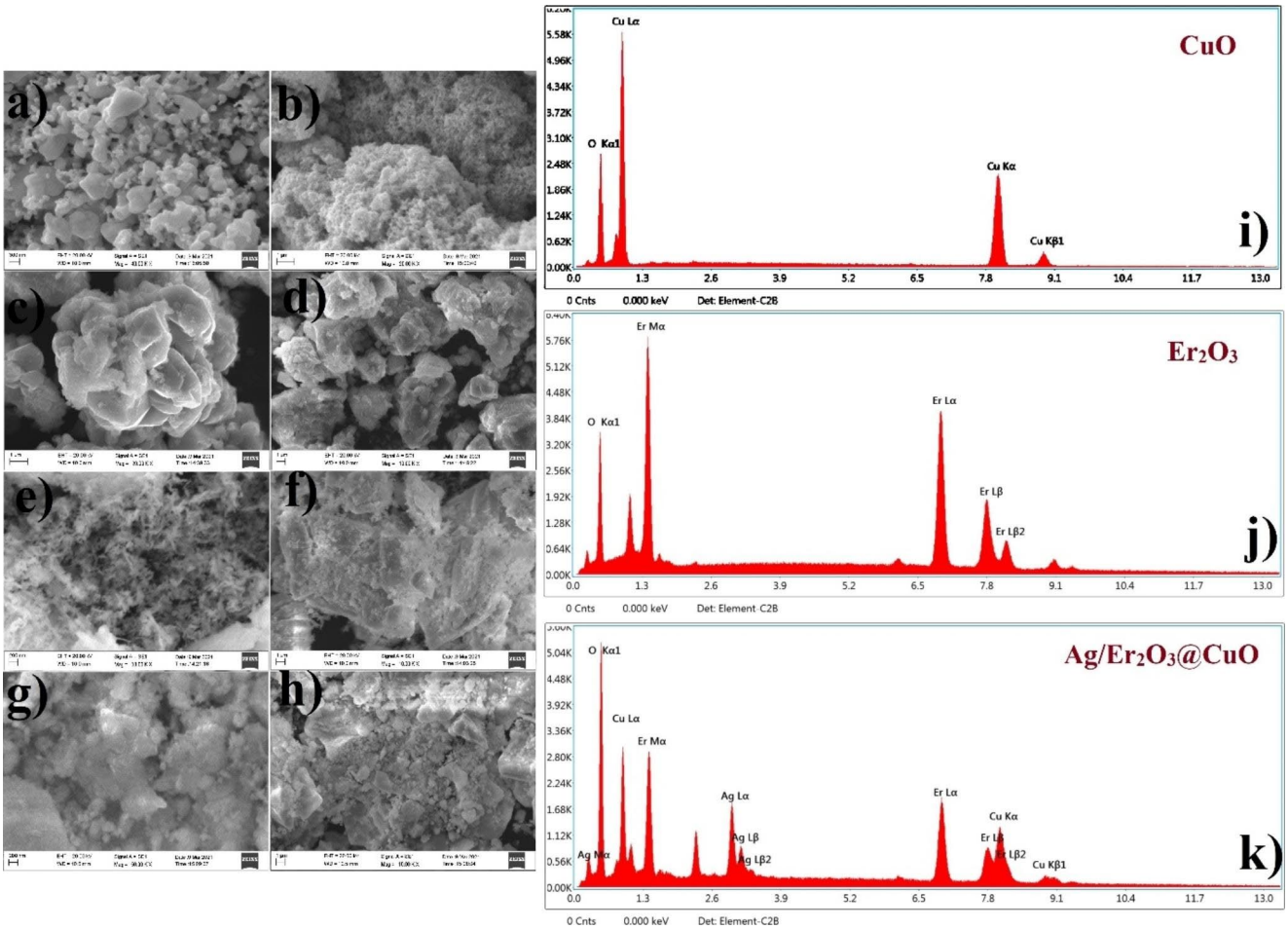

Fig. 3 SEM micrographs of (**a, b**) Ag; (**c, d**) CuO; (**e, f**) Er_2O_3 (**g, h**) Ag/Er_2O_3@CuO nanomaterial and (**i, j, k**) represents the EDX spectrum of CuO, Er_2O_3 and Ag/Er_2O_3@CuO nanomaterials

respectively (Fig. S2). The mesoporous nature and nanoscale size of the particles may have contributed to the large surface areas and increased porosity of our fabricated composites. According to Barrett-Joyner-Halenda (BJH) analysis, the Ag/Er_2O_3@CuO nanocomposites had an average pore size of 2.52 nm. Further, their porosity and average particle size significantly affected their antimicrobial capabilities, as they directly determined the surface area and number of available active sites for interactions with microorganisms.

3.6 Antibacterial Performance of Ag/Er_2O_3@CuO NPs

3.6.1 Disk Diffusion Study

Er_2O_3, CuO, and Ag/Er_2O_3@CuO nanocomposites were evaluated for their antibacterial properties against *Vibrio culture, Serratia marcescens, Hemophilus influenzae*, and *Aeromonas*. Efficacy against Gram-negative and Gram-positive bacteria was shown for the Er_2O_3, CuO, and Ag/Er_2O_3@CuO nanocomposites. Ag was responsible for the improved antibacterial activity of the prepared nanocomposites. Some studies have found that silver has high antibacterial activity. Several studies have reported the mechanisms by which silver exerts its potent antibacterial effects. As shown in Fig. 5(a), Er_2O_3, CuO, and Ag/Er_2O_3@CuO effectively killed the various bacteria. Compared to Ag/Er_2O_3@CuO, the zones of inhibition were larger against *Hemophilus influenzae*, and *Aeromonas*. These bacteria were more sensitive due to the larger inhibition zones between the activities of the nanocomposites. The silver (Ag) in the nanocomposites is a major factor in the superior performance of the Ag/Er_2O_3@CuO zones. The MIC values for both species (Table 1) were the same because of the contribution of Ag to the nanocomposites. Ag/Er_2O_3@CuO showed greater activity than the other catalysts because its zones were larger in most cases. Figure 5(b) shows how the Ag/Er_2O_3@CuO nanocomposite exerts its antibacterial action against a wide range of bacterial pathogens.

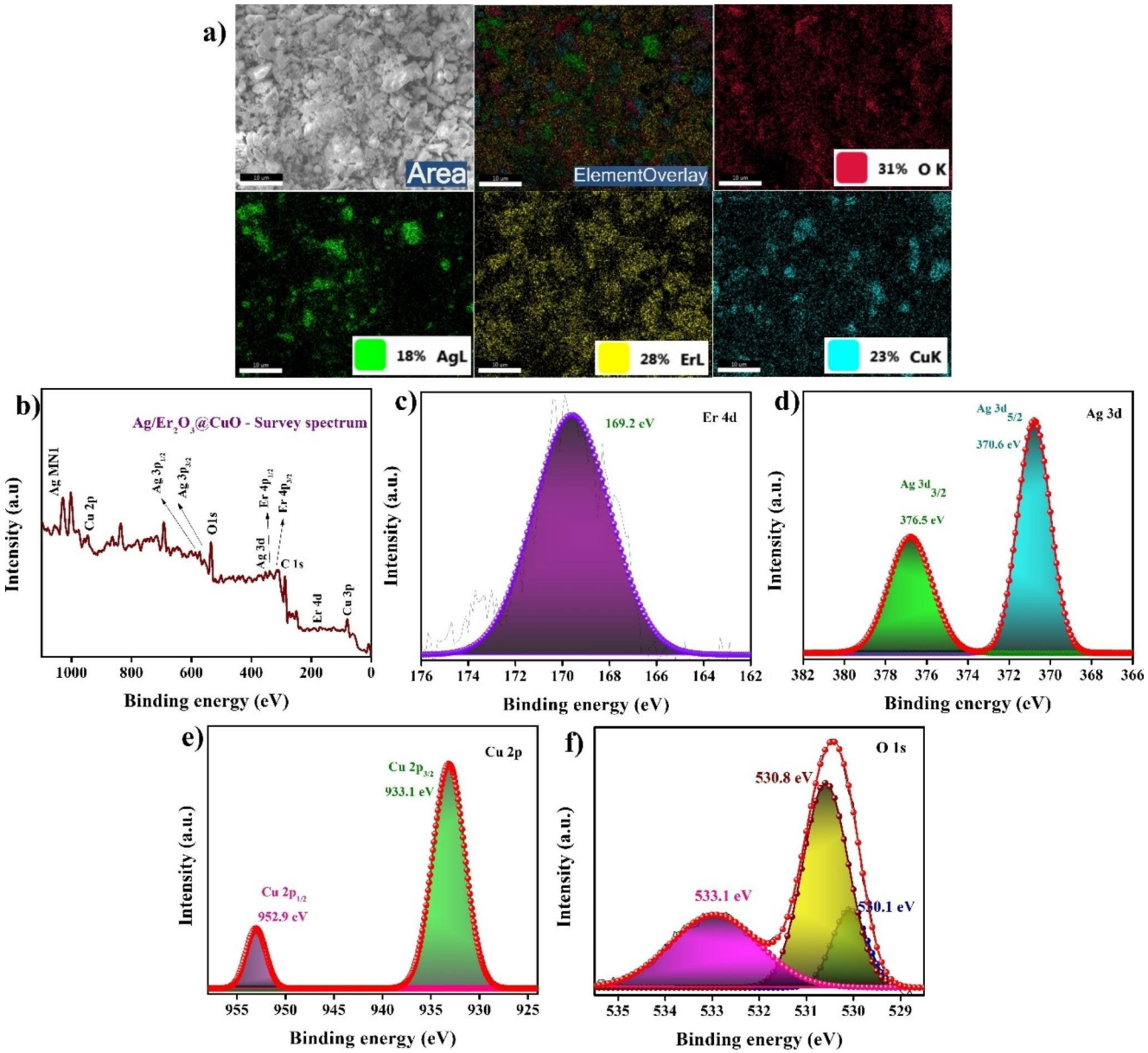

Fig. 4 (**a**) Color mapping images of as presenting elements for Ag/Er_2O_3@CuO nanomaterial and XPS spectrum of as prepared Ag/Er_2O_3@CuO nanocomposite; (**b**) survey scan spectrum, (**c**) Er 4d, (**d**) Ag 3d, (**e**) Cu 2p and (**f**) O 1s

3.7 Photocatalytic Performance of Pollutants

3.7.1 Prediction of Catalyst Usage Level

The degradation conditions for organic pollutants were determined by determining the sweet spot for a number of parameters such as nanomaterial dosage level, different nanomaterial usages (host and doped), concentrations of pollutants, scavengers, and the cycle of the degradation test. Figure 6 (b) shows how multiple catalysts, including the host Er_2O_3 and CuO, and the combination material Ag/Er_2O_3@CuO, were optimized for use with both AM dyes. It was found that the photocatalyst with the highest degradation ability degraded the AM dye in less than an hour and that the concentration of the pollutant dropped to nearly zero. In addition, the degradation efficacy of the other host materials was much lower than that of Ag/Er_2O_3@CuO, and complete mineralization did not occur. Thus, Ag/Er_2O_3@CuO materials are significantly more effective as host catalysts than competing materials.

In Fig. 6a, the visible-light absorption value of Amaranth (AM) (1×10^{-5} M) dye is shown in the presence of Ag/Er_2O_3@CuO nanomaterial [30 mg/L]. The rate constants obtained from the kinetic parameters are depicted in

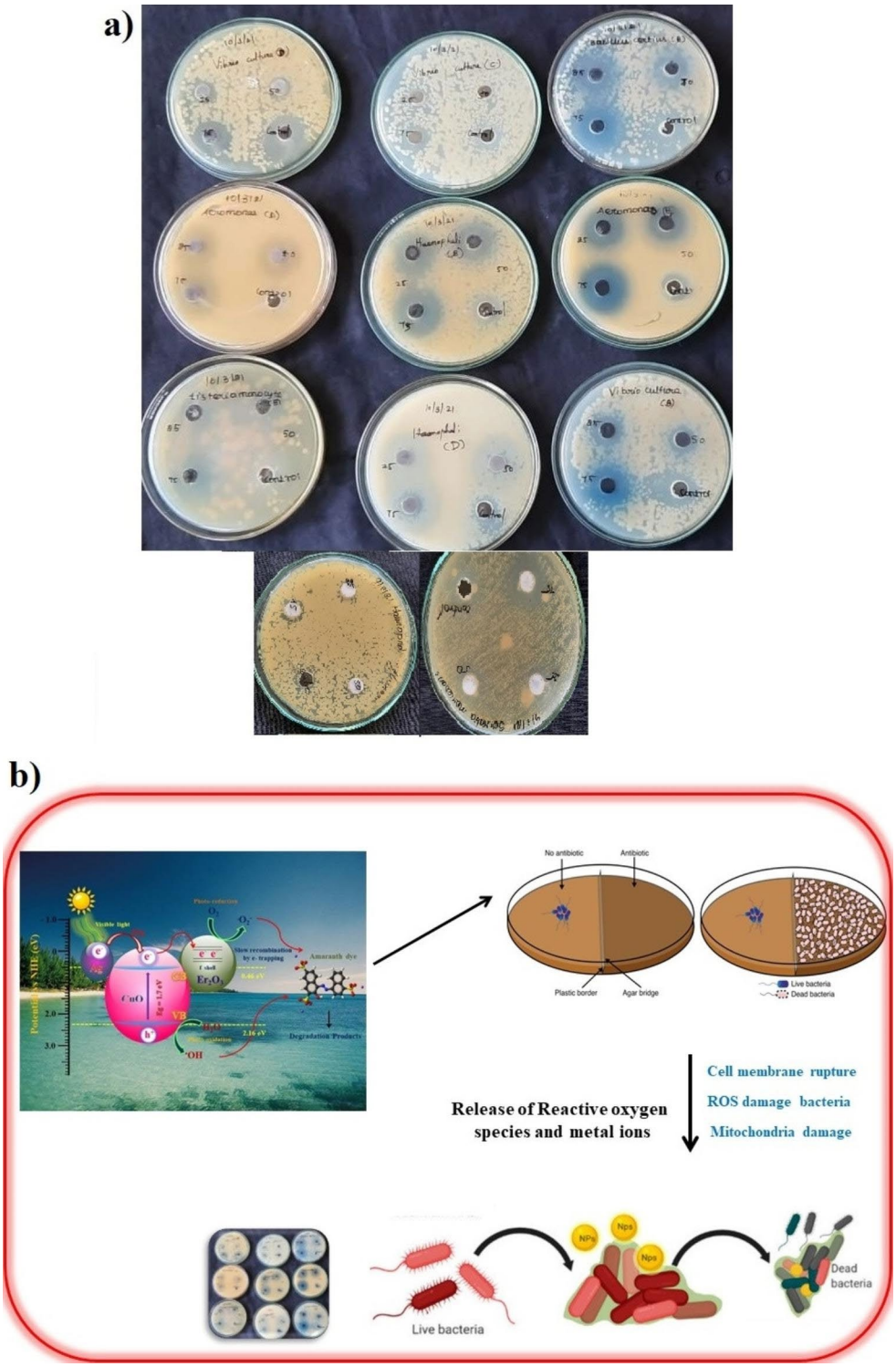

Fig. 5 (**a**) Antibacterial activity of Er_2O_3, CuO and Ag/Er_2O_3@CuO nanocomposite against various bacterial pathogens and (**b**) antibacterial activity mechanism of Ag/Er_2O_3@CuO nanocomposite against various bacterial pathogens

Fig. 6c, and the results are reported in Table 2 for both the host and the Ag/Er_2O_3@CuO nanocomposites. Overall, the Ag/Er_2O_3@CuO nanocomposites exhibited superior catalytic efficiency compared to other host materials, such as Er_2O_3, CuO, and Er_2O_3@CuO (Fig. S3).

3.7.2 Optimization of CIP and MO Concentration

An essential part of the degradation process is the optimization of the pollutant concentration. The efficiency of the photocatalyst can be enhanced by considering the starting concentration of the AM. The AM dye concentrations varied

Table 1 In-vitro Antibacterial activity of Ag/Er_2O_3@CuO nanomaterials

	Samples	Total Zone of Inhibition (cm)								
		Er_2O_3**(C)**			CuO **(B)**			Ag/Er_2O_3@CuO **(D)**		
	Bacteria	**25%**	**50%**	**75%**	**25%**	**50%**	**75%**	**25%**	**50%**	**75%**
Clear Zone diameter (cm)	Vibrio culture (GN)	1.3	1.4	1.6	1.4	1.5	1.8	1.3	1.9	2
	Serratia marcescens (GN)	-	-	-	1.1	1.5	2	1.7	2	2.4
	Haemophilus influenza (GN)	1.3	1.6	1.8	1.8	2	2.5	2.4	2.5	2.6
	Aeromonas (GN)	0.3	0.4	0.6	1.0	1.2	1.5	2.3	2	2.6

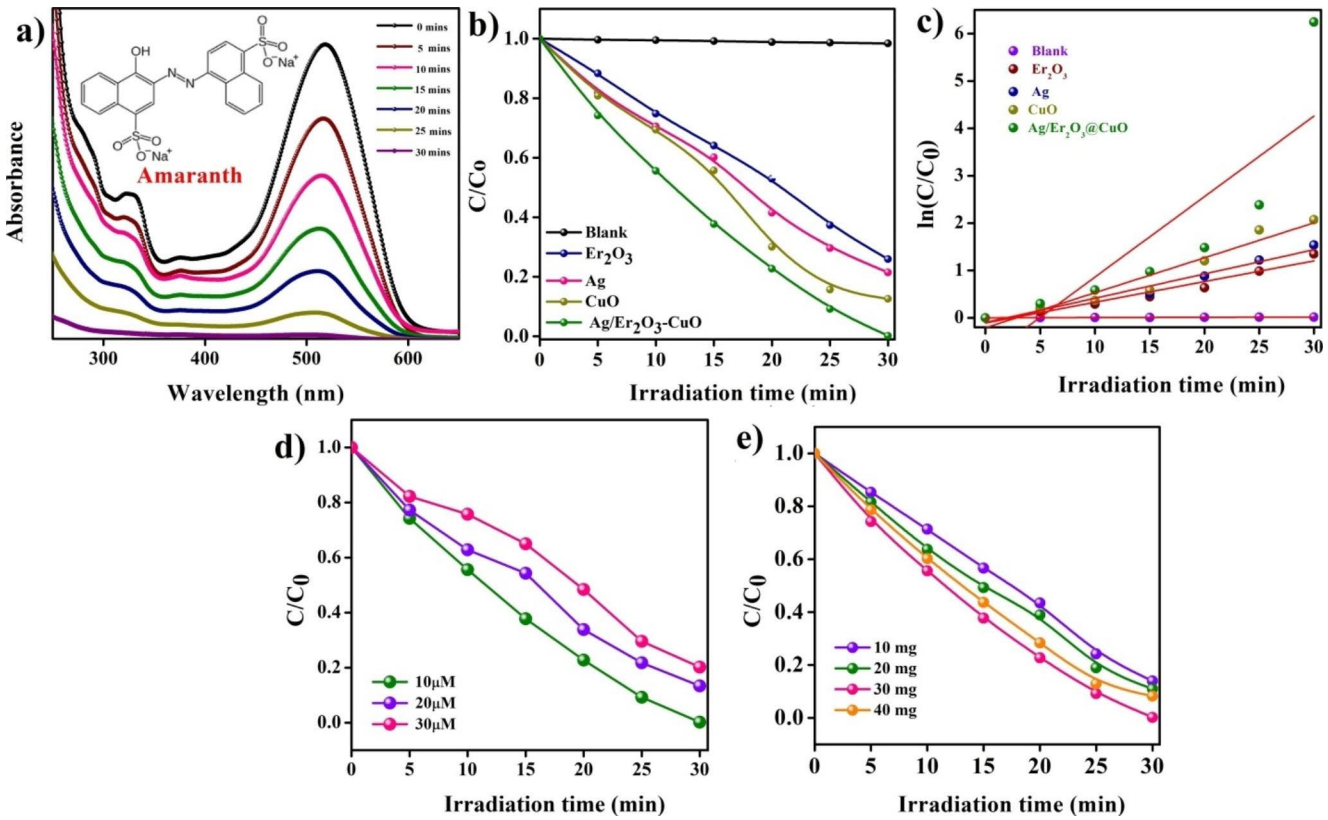

Fig. 6 Photodegradation of AM dye (**a**) Absorption spectrum of AM dye, (**b**) Photodegradation of AM dye using various catalysts and (**c**) The kinetics plot for various catalysts, (**d, e**) photodegradation of AM dye solution under different conditions: (**d**) Optimization concentration of AM dye, (**e**) Optimized catalyst dosage by AM degradation

Table 2 The Kinetics parameters for the photocatalytic degradation of amaranth (AM) Organic pollutant under visible light irradiation with various catalysts

S. No	Catalysts	Degradation efficiency (%)	Apparent rate constants k (min^{-1})	
		MO	R^2	k_{app}
1.	Blank	1.61	0.9934	5.332 E^{-4}
2.	Er_2O_3	74.07	0.9467	0.0437
3.	Ag	78.53	0.9649	0.0573
4.	CuO	87.43	0.9326	0.0739
5.	Ag/Er_2O_3@CuO	98.3	0.6737	0.1701

between 10 and 30 µM, while all other variables were held constant. There may not be enough photons available for the breakdown and surface of the light catalyst at high concentrations of pollutants, causing the photocatalytic reaction rate to drop dramatically. As shown in Fig. 6d, the optimal AM concentration was 10 µM.

3.7.3 Optimization of Catalyst Dosage

Catalyst dose optimization is an important process variable for the deterioration of composite materials. The catalyst dosages ranged from to 10–30 mg/L for AM, and their effects on organic pollutant degradation were studied (Fig. 6e). The decomposition of AM was rapid up to a dose of 30 mg/L of Ag/Er_2O_3@CuO and then began to slow. The

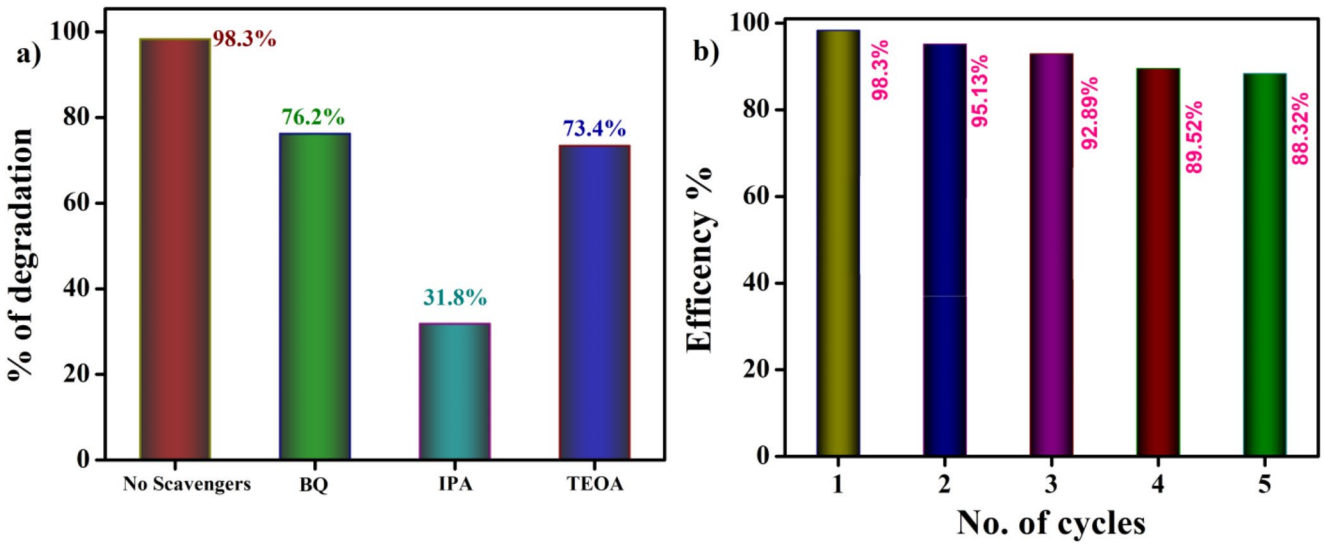

Fig. 7 (**a**) Reactive oxidative species study with different scavengers and (**b**) recycle ability test of Ag/Er_2O_3@CuO nanocomposite for AM dye degradation

number of reaction sites for photosynthesis can be increased by increasing the photocatalyst concentration. However, the breakdown efficiency decreases dramatically when the photosynthetic dosage is increased, as this increases the integration of nano-photocatalysts and decreases their active surface areas. Additionally, an increase in the turbulence of the solution can prevent more light from passing through.

3.7.4 Degradation Mechanism and ROS Studies

The scavengers used for benzoquinone (BQ), triethanolamine (TEOA), ethanol, and isopropanol (IPA) in this study were superoxide (O_2^{*-}), hole (h^+), electron (e^-), and hydroxyl ($^{\bullet}OH$) radicals [69–74]. From the reactive oxygen species (ROS) study, superoxide radical (O_2^{*-}) and hydroxyl group ($^{*}OH$) scavengers were efficiently formed via this method by interacting with O_2 groups and H_2O molecules on the catalyst surface. As shown in Fig. 7a, the primary species involved in the inhibition of this degradation were hydroxyl group ($^{*}OH$) scavengers. Charge transfer processes under visible-light irradiation generate radical species that degrade contaminants. Because of the low bandgap of CuO, visible-light photons excite electrons in the valence band (VB), moving them into the conduction band (CB) and leaving holes in the former. Er_2O_3 is then used as a photoelectronic acceptor, and the photogenerated electrons in CuO's CB are swiftly transferred to Er_2O_3's CB. Superoxide radical anions ($O_2 + e^- \rightarrow O_2^{\cdot -}$) are formed when oxygen accepts photo-induced electrons. The result of this process is that harmful organic substances in the wastewater are eliminated, and more oxygen species are produced through different interactions with h^+. Water can be oxidized into hydroxyl radicals ($H_2O + h^+ \rightarrow OH^{\cdot}$) during this process of concurrent hole transport in the opposite direction. The primary products of the chemical interactions between the highly oxidizing hydroxyl radicals and organic matter molecules are carbon dioxide (CO_2) and water (H_2O) (Fig. 8). This phenomenon is represented by Eq. S1-S7. The electron hole pairs in the photocatalyst's CB and VB are respectively denoted as e^-_{CB} and h_{VB}^+. According to Eq. S1, the catalyst can create e^- - h^+ pairs under light irradiation. The migrated electrons then react with O_2 to form $O_2^{\cdot -}$ (Eq. S2), thus preventing electron-hole pairs created by light from recombining. Next, the produced superoxide radicals react with H^+ to form .OH (Eq. S3), and the photogenerated electrons react with oxygen to form hydroxide ions (Eq. S4). According to Eq. S5-S7, the decomposition of the adsorbed dye molecules on the photocatalyst surface could also have been caused by photogenerated holes in the VB, which can lead to radical cation formation. Parallelly, electron holes can also react with hydroxide ions to produce $HO^{\cdot}$, which could further accelerate the breakdown of the dye. Therefore, the efficient breakdown of dyes can be attributed to the active radical species.

Ultraviolet photoelectron spectroscopy (UPS) was used to determine the VB and CB of the photocatalytic materials. As illustrated in Fig. S4, the secondary electron cut-off can be used to obtain the high-binding-energy cutoff (E_{cutoff}), and the VB region can be used to obtain the onset energy (E_{onset}). Both parameters were determined using a secondary electron cut-off value. For the testing apparatus, the incident photon energy, $E_{incident}$, was determined to be 21.11 eV. The following valence band maximum (VBM) equation [75] explains this outcome:

$$\mathrm{VBM} = E_{incident} - (E_{cutoff} - E_{onset})$$

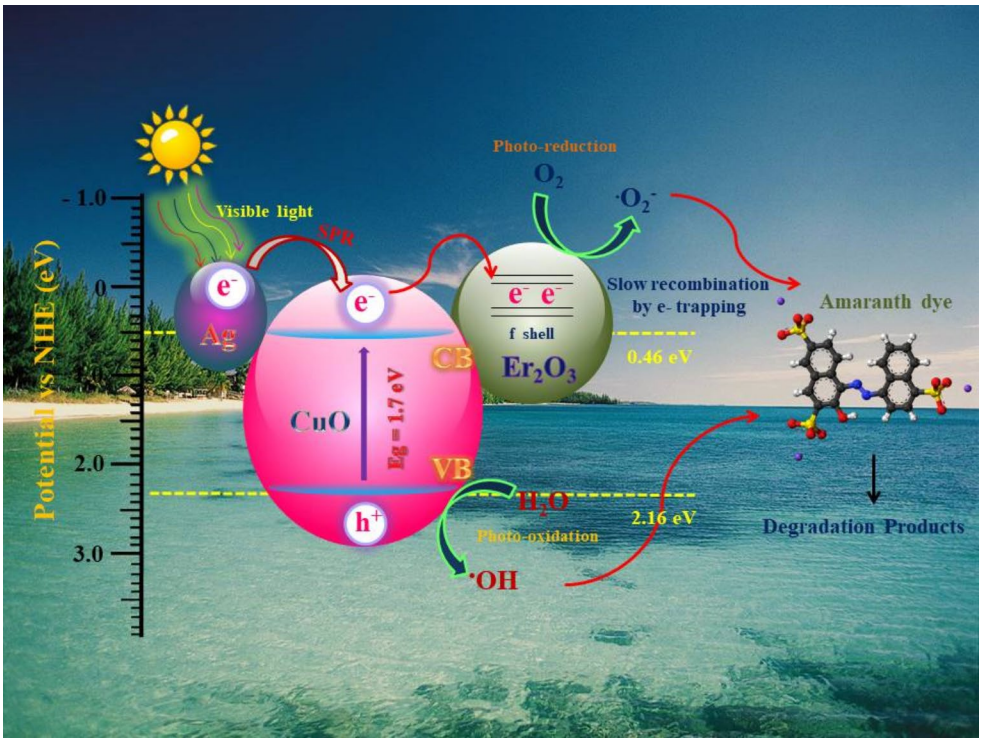

Fig. 8 Schematic representation for photocatalytic mechanism of Ag/Er_2O_3@CuO nanocomposite

Our calculations indicated that the VBM of Er_2O_3 was 8.26 eV below the vacuum level. In conjunction with the bandgap value of 5.3 eV, generated from the DRS-UV spectra [76], the level of the conduction band maximum (CBM) was estimated to reside 2.96 eV below the vacuum level for Er_2O_3. In addition, the CB and VB of Er_2O_3 were determined (Supporting Information). When Er_2O_3 was coupled with CuO, the band energy decreased, indicating that they can be excited via visible light irradiation. The doped Er_2O_3 causes electron separation and inhibits recombination in CuO, allowing electrons to move from the VB to the CB upon irradiation [77].

3.7.5 Photocatalyst Recyclability

These recycling tests revealed the stability and recyclability of the as-obtained catalysts, which are critical for decomposition. The used catalyst was recovered after the first deterioration cycle and returned to the recycling test after another six degradation cycles under the optimized conditions. Figure 7b, indicates that a moderate decrease in photosynthetic efficiency occurred when the attenuation of the AM dye was increased. Compared to other CuO and Er_2O_3 catalysts, Ag/Er_2O_3@CuO has a superior degradation efficiency [78–87], the results demonstrated in Table 3. Fig. S5

Table 3 The comparison of Ag/Er_2O_3@CuO nanocomposite with some other previous reports of Er_2O_3 and CuO based photocatalyst for degradation process

S. No	Catalyst	Weight of catalyst (g/L)	Organic pollutant	Irradiation source	% of degradation	Degradation time (min)	Reference
1	$(Er_2O_3)_x(Yb_2O_3)_y(Bi_2O_3)_{1-x-y}$	4	CV	UV light	50.1	180	[78]
2	ZnO/CuO	0.02	MB	Visible light	76	150	[79]
3	CuO Coated ZnO	0.15	4-NP	Sun light	93	180	[80]
4	Er_2O_3/ZnO@Mo	0.05	MB	UV light	80	120	[81]
5	Er_2O_3-coated silicon nanowires	-	MB	UV light	99	90	[82]
6	Z-scheme ZnO-Er_2O_3-Nd_2O_3@rGO	0.03	MB	Sun light	97	60	[83]
7	CuO-Ag-ZnO	0.02	MO	Visible light	96.3	30	[84]
8	Ag–CuO–ZnO	0.03	MO	Visible light	98	60	[85]
9	Ni-doped CuO/Fe_2O_3	0.125	MB	Visible light	94	120	[86]
10	Ag/CuO/WO_3	0.05	AR 88	Visible light	90	180	[87]
11	Ag/Er_2O_3@CuO	0.03	AM	Visible light	98.3	30	Present work

shows that after 30 min of irradiation, the Ag/Er_2O_3@CuO photocatalytic system attained the 56.5% mineralization of the AM dye (TOC removal).

4 Conclusion

In this study, a new Ag/Er_2O_3@CuO composite with antibacterial properties was successfully synthesized via hydrothermal synthesis, where spherical Ag particles were well-deposited on the Er_2O_3@CuO composite. The composites with 25%, 50%, and 75% CuO, Er_2O_3, and Ag/Er_2O_3@CuO exhibited notable clear zones of antibacterial activity against *Hemophilus influenza* and *Aeromonas*, with the Ag/Er_2O_3@CuO composite showcasing the most favorable inhibition zone compared to those of the other host materials. Furthermore, the enhanced photocatalytic properties of the Ag/Er_2O_3@CuO nanocomposite led to an AM dye degradation efficiency of over 98%. Furthermore, the optimal parameters for the Ag/Er_2O_3@CuO nanoparticles were studied.

Supplementary Information The online version contains supplementary material available at https://doi.org/10.1007/s10904-023-02802-w.

Acknowledgements This work was supported by the National Research Foundation of Korea (NRF) grant funded by the Korea government (MSIT) (No. 2022R1A2C1004283) and the authors thank the Core Research Support Center for Natural Products and Medical Materials (CRCNM) in Yeungnam University.

Author Contributions M. Arunpandian: Conceptualization, Investigation, Writing - original draft, Data curation. L.T. Parvathi: Investigation, Data curation. K. Selvakumar: Methodology, Investigation. Tae Hwan Oh: Supervision, Writing - review & editing. S. Karuthapandian: Data curation, Methodology, Investigation. All authors read and approved the final manuscript.

Declarations

Conflict of interest There is no conflict of interest between the authors.

References

1. K. Glinel, A.M. Jonas, T. Jouenne, J. Leprince, L. Galas, W.T. Huck, Antibacterial and antifouling polymer brushes incorporating antimicrobial peptide. Bioconjug. Chem. **20**, 71–77 (2009)
2. E.M. Hetrick, M.H. Schoenfisch, Reducing implant-related infections: active release strategies. Chem. Soc. Rev. **35**, 780–789 (2006)
3. F. Costa, I.F. Carvalho, R.C. Montelaro, P. Gomes, M.C.L. Martins, Covalent immobilization of antimicrobial peptides (AMPs) onto biomaterial surfaces. Acta Biomater. **7**, 1431–1440 (2011)
4. H.A. Durr, N.D. Leipzig, Advancements in bacteriophage therapies and delivery for bacterial infection. Mater. Adv. **4**, 1249–1257 (2023)
5. E. Albalghiti, L.M. Stabryla, L.M. Gilbertson, J.B. Zimmerman, Towards resolution of antibacterial mechanisms in metal and metal oxide nanomaterials: a meta-analysis of the influence of study design on mechanistic conclusions. Environ. Science: Nano. **8**, 37–66 (2021)
6. J.A. Lemire, J.J. Harrison, R.J. Turner, Antimicrobial activity of metals: mechanisms, molecular targets and applications. Nat. Rev. Microbiol. **11**, 371–384 (2013)
7. D. Das, B.C. Nath, P. Phukon, S.K. Dolui, Synthesis of ZnO nanoparticles and evaluation of antioxidant and cytotoxic activity. Colloids Surf., B **111**, 556–560 (2013)
8. A. Rana, S. Pathak, D.K. Lim, S.K. Kim, R. Srivastava, S.N. Sharma, R. Verma, *Recent Advancements in Plant and Microbe Mediated Synthesis of Metal and Metal Oxide Nanomaterials and Their Emerging Antimicrobial Applications* (ACS Applied Nano Materials, 2023)
9. P. Prabhakaran, M.A. Ashraf, W.S. Aqma, Microbial stress response to heavy metals in the environment. RSC Adv. **6**, 109862–109877 (2016)
10. A. Rauf, J. Ye, S. Zhang, Y. Qi, G. Wang, Y. Che, G. Ning, Copper(ii)-based coordination polymer nanofibers as a highly effective antibacterial material with a synergistic mechanism. Dalton Trans. **48**, 17810–17817 (2019)
11. S. Soren, S. Kumar, S. Mishra, P.K. Jena, S.K. Verma, P. Parhi, Evaluation of antibacterial and antioxidant potential of the zinc oxide nanoparticles synthesized by aqueous and polyol method. Microb. Pathog. **119**, 145–151 (2018)
12. L. Zhang, L. Wu, Y. Mi, Y. Si, Silver nanoparticles induced cell apoptosis, membrane damage of Azotobacter vinelandii and Nitrosomonas europaea via generation of reactive oxygen species. Bull. Environ Contam. Toxicol. **103**, 181–186 (2019)
13. B.L. da Silva, B.L. Caetano, B.G. Chiari-Andréo, R.C.L.R. Pietro, L.A. Chiavacci, Increased antibacterial activity of ZnO nanoparticles: influence of size and surface modification. Colloids Surf., B **177**, 440–447 (2019)
14. A. Gholami, F. Mohammadi, Y. Ghasemi, N. Omidifar, A. Ebrahiminezhad, Antibacterial activity of SPIONs versus ferrous and ferric ions under aerobic and anaerobic conditions: a preliminary mechanism study. IET Nanobiotechnol. **14**, 155–160 (2020)
15. J.A. Lemire, R.J. Turner, Mechanisms underlying the antimicrobial capacity of metals, stress and environmental regulation of Gene expression and adaptation in Bacteria, (2016) 215–224
16. S.M. Baumler, G.J. Blanchard, The Influence of metal ions on the dynamics of supported phospholipid Langmuir films, Langmuir, 33 (2017) 2986–2992
17. K. Gold, B. Slay, M. Knackstedt, A.K. Gaharwar, Antimicrobial activity of metal and metal-oxide based nanoparticles. Adv. Ther. **1**, 1700033 (2018)
18. S. Cheeseman, A.J. Christofferson, R. Kariuki, D. Cozzolino, T. Daeneke, R.J. Crawford, V.K. Truong, J. Chapman, A. Elbourne, Antimicrobial metal nanomaterials: from passive to stimuli-activated applications. Adv. Sci. **7**, 1902913 (2020)
19. M. Mohammadi, M. Ghorbani, D. Fray, Preparation and characterisation of nanostructural TiO_2–Er_2O_3 binary oxides with high surface area derived from particulate sol–gel route. Mater. Sci. Technol. **22**, 965–974 (2006)
20. A. Trinchi, Y. Li, W. Wlodarski, S. Kaciulis, L. Pandolfi, S. Viticoli, E. Comini, G. Sberveglieri, Investigation of sol–gel prepared CeO_2–TiO_2 thin films for oxygen gas sensing. Sens. Actuators B **95**, 145–150 (2003)
21. Q. Zhang, K. Zhang, D. Xu, G. Yang, H. Huang, F. Nie, C. Liu, S. Yang, CuO nanostructures: synthesis, characterization, growth mechanisms, fundamental properties, and applications. Prog. Mater. Sci. **60**, 208–337 (2014)
22. M.M. Rahman, H.B. Balkhoyor, A.M. Asiri, Removal of a melamine contaminant with Ag-doped ZnO nanocomposite materials. New J. Chem. **43**, 18848–18859 (2019)
23. S. Kerli, Boron-doped cobalt oxide thin films and its electrochemical properties. Mod. Phys. Lett. B **30**, 1650343 (2016)

24. S.T. Jun, G.M. Choi, Composition dependence of the electrical conductivity of ZnO (n)–CuO (p) ceramic composite. J. Am. Ceram. Soc. **81**, 695–699 (1998)
25. P. Siriwong, T. Thongtem, A. Phuruangrat, S. Thongtem, Hydrothermal synthesis, characterization, and optical properties of wolframite $ZnWO_4$ nanorods, CrystEngComm, **13** (2011) 1564–1569
26. S. Pinchujit, A. Phuruangrat, S. Wannapop, T. Sakhon, B. Kuntalue, T. Thongtem, S. Thongtem, Synthesis and characterization of heterostructure Pt/Bi_2WO_6 nanocomposites with enhanced photodegradation efficiency induced by visible radiation. Solid State Sci. **134**, 107064 (2022)
27. A. Phuruangrat, S. Wannapop, T. Sakhon, B. Kuntalue, T. Thongtem, S. Thongtem, Characterization and photocatalytic properties of $BiVO_4$ synthesized by combustion method. J. Mol. Struct. **1274**, 134420 (2023)
28. O. Yayapao, T. Thongtem, A. Phuruangrat, S. Thongtem, Synthesis and characterization of highly efficient gd doped ZnO photocatalyst irradiated with ultraviolet and visible radiations. Mater. Sci. Semiconduct. Process. **39**, 786–792 (2015)
29. K. Chen, D. Xue, Formation of electroactive colloids via in situ coprecipitation under electric field: erbium chloride alkaline aqueous pseudocapacitor. J. Colloid Interface Sci. **430**, 265–271 (2014)
30. M. Govindasamy, S.M. Chen, V. Mani, R. Devasenathipathy, R. Umamaheswari, K. Joseph Santhanaraj, A. Sathiyan, Molybdenum disulfide nanosheets coated multiwalled carbon nanotubes composite for highly sensitive determination of chloramphenicol in food samples milk, honey and powdered milk. J. Colloid Interface Sci. **485**, 129–136 (2017)
31. M. Govindasamy, U. Rajaji, S.M. Chen, S. Kumaravel, T.W. Chen, F.M.A. Al Hemaid, M.A. Ali, M.S. Elshikh, Detection of Pesticide residues (Fenitrothion) in Fruit samples based on Niobium Carbide@Molybdenum Nanocomposite: an Electrocatalytic Approach. Anal. Chim. Acta. **1030**, 52–60 (2018)
32. C.H. Liang, M.F. Hou, S.G. Zhou, F.B. Li, C.S. Liu, T.X. Liu, Y.X. Gao, X.G. Wang, J.L. Lü, The effect of erbium on the adsorption and photodegradation of orange I in aqueous Er^{3+}-TiO_2 suspension. J. Hazard. Mater. **138**, 471–478 (2006)
33. K. Chen, D. Xue, Rare earth and transitional metal colloidal supercapacitors. Sci. China Technological Sci. **58**, 1768–1778 (2015)
34. M.R. Ganjali, F. Faridbod, P. Norouzi, M. Adib, A novel Er(III) sensor based on a new hydrazone for the monitoring of Er(III) ions. Sens. Actuators B **120**, 119–124 (2006)
35. S. Obregón, G. Colón, Heterostructured Er^{3+} doped $BiVO_4$ with exceptional photocatalytic performance by cooperative electronic and luminescence sensitization mechanism. Appl. Catal. B **158**, 242–249 (2014)
36. S. Obregón, S.W. Lee, G. Colón, Exalted photocatalytic activity of tetragonal $BiVO_4$ by Er^{3+} doping through a luminescence cooperative mechanism. Dalton Trans. **43**, 311–316 (2014)
37. N. Mir, *Rare earth–doped Semiconductor Nanomaterials, Advanced Rare Earth-Based Ceramic Nanomaterials* (Elsevier, 2022), pp. 291–338
38. T. Gnanasekar, S. Valanarasu, M. Ubaidullah, M. Alam, A. Nafady, P. Mohanraj, I.L. Poul Raj, T. Ahmad, M. Shahazad, B. Pandit, Fabrication of Er, Tb doped CuO thin films using nebulizer spray pyrolysis technique for photosensing applications. Opt. Mater. **123**, 111954 (2022)
39. S. Jammi, S. Sakthivel, L. Rout, T. Mukherjee, S. Mandal, R. Mitra, P. Saha, T. Punniyamurthy, CuO nanoparticles catalyzed C – N, C – O, and C – S cross-coupling reactions: scope and mechanism. J. Org. Chem. **74**, 1971–1976 (2009)
40. D. Das, B.C. Nath, P. Phukon, S.K. Dolui, Synthesis and evaluation of antioxidant and antibacterial behavior of CuO nanoparticles. Colloids Surf., B **101**, 430–433 (2013)
41. J. Zhao, Z. Wang, Y. Dai, B. Xing, Mitigation of CuO nanoparticle-induced bacterial membrane damage by dissolved organic matter. Water Res. **47**, 4169–4178 (2013)
42. K. Zhou, R. Wang, B. Xu, Y. Li, Synthesis, characterization and catalytic properties of CuO nanocrystals with various shapes. Nanotechnology. **17**, 3939 (2006)
43. J.W. Ko, S.W. Kim, J. Hong, J. Ryu, K. Kang, C.B. Park, Synthesis of graphene-wrapped CuO hybrid materials by CO_2 mineralization. Green Chem. **14**, 2391–2394 (2012)
44. S. Chandrasekaran, A novel single step synthesis, high efficiency and cost effective photovoltaic applications of oxidized copper nano particles. Sol. Energy Mater. Sol. Cells. **109**, 220–226 (2013)
45. J. Huang, H. Wu, D. Cao, G. Wang, Influence of Ag doped CuO nanosheet arrays on electrochemical behaviors for supercapacitors. Electrochim. Acta. **75**, 208–212 (2012)
46. A. Aslani, V. Oroojpour, CO gas sensing of CuO nanostructures, synthesized by an assisted solvothermal wet chemical route. Phys. B: Condens. Matter. **406**, 144–149 (2011)
47. X. Zhang, G. Wang, X. Liu, J. Wu, M. Li, J. Gu, H. Liu, B. Fang, Different CuO nanostructures: synthesis, characterization, and applications for glucose sensors. J. Phys. Chem. C **112**, 16845–16849 (2008)
48. K. Reddy, T. Roth, Arsenic removal from natural groundwater using cupric oxide. Groundwater. **51**, 83–91 (2013)
49. K.M. Kim, H.M. Jeong, H.R. Kim, K.-I. Choi, H.J. Kim, J.H. Lee, Selective detection of NO_2 using Cr-doped CuO nanorods. Sensors. **12**, 8013–8025 (2012)
50. Z. Yang, J. Feng, J. Qiao, Y. Yan, Q. Yu, K. Sun, Copper oxide nanoleaves decorated multi-walled carbon nanotube as platform for glucose sensing. Anal. Methods. **4**, 1924–1926 (2012)
51. M. Suleiman, M. Mousa, A. Hussein, B. Hammouti, T.B. Hadda, I. Warad, Copper (II)-oxide nanostructures: synthesis, characterizations and their applications-review. J. Mater. Environ. Sci. **4**, 792–797 (2013)
52. D.F. Ollis, Photocatalytic purification and remediation of contaminated air and water, Comptes Rendus de l'Académie des Sciences - Series IIC - Chemistry, 3 (2000) 405–411
53. P. Raizada, A. Sudhaik, S. Patial, V. Hasija, A.A. Parwaz Khan, P. Singh, S. Gautam, M. Kaur, V.-H. Nguyen, Engineering nanostructures of CuO-based photocatalysts for water treatment: current progress and future challenges. Arab. J. Chem. **13**, 8424–8457 (2020)
54. K.I. Zamaraev, *Photocatalysis: State of the art and Perspectives, Studies in Surface Science and Catalysis* (Elsevier, 1996), pp. 35–50
55. G. Mele, E. Garcìa-Lòpez, L. Palmisano, G. Dyrda, R. Słota, Photocatalytic degradation of 4-nitrophenol in aqueous suspension by using polycrystalline TiO_2 impregnated with lanthanide double-decker phthalocyanine complexes. J. Phys. Chem. C **111**, 6581–6588 (2007)
56. M.R. Hoffmann, S.T. Martin, W. Choi, D.W. Bahnemann, Environmental applications of semiconductor photocatalysis. Chem. Rev. **95**, 69–96 (1995)
57. M. Yasmina, K. Mourad, S.H. Mohammed, C. Khaoula, Treatment heterogeneous photocatalysis; factors influencing the photocatalytic degradation by TiO_2. Energy Procedia. **50**, 559–566 (2014)
58. S. Esplugas, J. Gimenez, S. Contreras, E. Pascual, M. Rodríguez, Comparison of different advanced oxidation processes for phenol degradation. Water Res. **36**, 1034–1042 (2002)
59. M. Pera-Titus, V. García-Molina, M.A. Baños, J. Giménez, S. Esplugas, Degradation of chlorophenols by means of advanced oxidation processes: a general review. Appl. Catal. B **47**, 219–256 (2004)

60. S.G. Kumar, K.K. Rao, Zinc oxide based photocatalysis: tailoring surface bulk structure and related interfacial charge carrier dynamics for better environmental applications. RSC Adv. **5**, 3306–3351 (2015)
61. M. Arunpandian, K. Selvakumar, A. Raja, M. Thiruppathi, P. Rajasekaran, P. Rameshkumar, E.R. Nagarajan, S. Arunachalam, Development of novel Nd_2WO_6/ZnO incorporated on GO nanocomposite for the photocatalytic degradation of organic pollutants and biological studies. J. Mater. Sci.: Mater. Electron. **30**, 18557–18574 (2019)
62. A. Hajnorouzi, Two ultrasonic applications for the synthesis of nanostructured copper oxide (II). Ultrason. Sonochem. **64**, 105020 (2020)
63. B. Kandasamy, S.B. Sussela, R. Sankararajan, P. Govindasamy, P. Thangavelu, V. Shanmugam, E. Nagaraj, V. Gopal, S. Manickam, R. Perumalsamy, Strontium-supported erbium oxide nanoparticles for efficient organic pollutant degradation under UV–Visible light. J. Mater. Sci.: Mater. Electron. **33**, 20384–20398 (2022)
64. F.A. Alharthi, A.A. Alghamdi, N. Al-Zaqri, H.S. Alanazi, A.A. Alsyahi, A.E. Marghany, N. Ahmad, Facile one-pot green synthesis of Ag–ZnO nanocomposites using potato peeland their ag concentration dependent photocatalytic properties. Sci. Rep. **10**, 20229 (2020)
65. N. Karikalan, R. Karthik, S.-M. Chen, C. Karuppiah, A. Elangovan, Sonochemical synthesis of sulfur doped reduced graphene oxide supported CuS nanoparticles for the non-enzymatic glucose sensor applications. Sci. Rep. **7**, 2494 (2017)
66. K. Upadhya, R. Kumar, M. Baral, S. Tripathi, S. Jha, T. Ganguli, B. Saha, Electronic structure of rare-earth semiconducting ErN thin films determined with synchrotron radiation photoemission spectroscopy and first-principles analysis. Phys. Rev. B **105**, 075138 (2022)
67. M. Michalska, J. Pavlovský, K. Lemański, M. Małecka, M. Ptak, V. Novák, M. Kormunda, V. Matějka, The effect of surface modification with Ag nanoparticles on 21 nm TiO_2: anatase/rutile material for application in photocatalysis. Mater. Today Chem. **26**, 101123 (2022)
68. M. Michalska, V. Matějka, J. Pavlovský, P. Praus, M. Ritz, J. Serenčíšová, L. Gembalová, M. Kormunda, K. Foniok, M. Reli, Simha Martynková, Effect of Ag modification on TiO_2 and melem/g-C_3N_4 composite on photocatalytic performances. Sci. Rep. **13**, 5270 (2023)
69. M. Arunpandian, K. Selvakumar, A. Raja, P. Rajasekaran, M. Thiruppathi, E.R. Nagarajan, S. Arunachalam, Fabrication of novel Nd_2O_3/ZnO-GO nanocomposite: an efficient photocatalyst for the degradation of organic pollutants. Colloids Surf., A **567**, 213–227 (2019)
70. A. Raja, P. Rajasekaran, K. Selvakumar, M. Arunpandian, K. Kaviyarasu, S. Asath Bahadur, M. Swaminathan, Visible active reduced graphene oxide-$BiVO_4$-ZnO ternary photocatalyst for efficient removal of ciprofloxacin. Sep. Purif. Technol. **233**, 115996 (2020)
71. K. Selvakumar, A. Raja, M. Arunpandian, K. Stalindurai, P. Rajasekaran, P. Sami, E.R. Nagarajan, M. Swaminathan, Efficient photocatalytic degradation of ciprofloxacin and bisphenol A under visible light using Gd_2WO_6 loaded ZnO/bentonite nanocomposite. Appl. Surf. Sci. **481**, 1109–1119 (2019)
72. A. Raja, K. Selvakumar, P. Rajasekaran, M. Arunpandian, S. Ashokkumar, K. Kaviyarasu, S.A. Bahadur, M. Swaminathan, Visible active reduced graphene oxide loaded titania for photodecomposition of ciprofloxacin and its antibacterial activity. Colloids Surf., A **564**, 23–30 (2019)
73. M. Arunpandian, K. Selvakumar, A. Raja, P. Rajasekaran, C. Ramalingan, E. Nagarajan, A. Pandikumar, S. Arunachalam, Rational design of novel ternary Sm_2WO_6/ZnO/GO nanocomposites: an affordable photocatalyst for the mitigation of carcinogenic organic pollutants. Colloids Surf., A **596**, 124721 (2020)
74. K. Selvakumar, Y. Wang, Y. Lu, B. Tian, Z. Zhang, J. Hu, A. Raja, M. Arunpandian, M. Swaminathan, H. Dai, Single metal atom oxide anchored Fe_3O_4-ED-rGO for highly efficient photodecomposition of antibiotic residues under visible light illumination. Appl. Catal. B **300**, 120740 (2022)
75. S. Ji, T. Shi, X. Qiu, J. Zhang, G. Xu, C. Chen, Z. Jiang, C. Ye, A route to phase controllable $Cu_2ZnSn(S_{(1-x)}Se_{(x)})_4$ nanocrystals with tunable energy bands. Sci. Rep. **3**, 2733 (2013)
76. T. Munawar, S. Yasmeen, A. Hussain, M. Akram, F. Iqbal, Novel direct dual-Z-scheme ZnO-Er_2O_3-Yb_2O_3 heterostructured nanocomposite with superior photocatalytic and antibacterial activity. Mater. Lett. **264**, 127357 (2020)
77. Z. Liu, J. Xu, Q. Liao, Y. Li, L. Li, M. Mao, Synthesis of Sm_2MoO_6/$Ni(OH)_2$ by simple impregnation method: Photocatalyst for non-precious metal and efficient hydrogen production. Catal. Lett. **150**, 39–48 (2020)
78. Z. Bilici, P. Guler, Y. Ozay, S. Yilmaz, H. Cengiz Yatmaz, N. Dizge, Photocatalytic activity of $(Er_2O_3)_x(Yb_2O_3)_y(Bi_2O_3)_{1-x-y}$ ternary compounds used as heterogeneous semiconductor. Mater. Sci. Engineering: B **271**, 115250 (2021)
79. N. Jalali, M. Nami, F. Rashchi, A. Rakhsha, Photocatalytic properties of ZnO/CuO nanocomposite prepared in acidic media. J. Ultrafine Grained Nanostructured Mater. **55**, 21–30 (2022)
80. M.T. Qamar, M. Aslam, I.M.I. Ismail, N. Salah, A. Hameed, Synthesis, characterization, and sunlight mediated photocatalytic activity of CuO Coated ZnO for the removal of Nitrophenols. ACS Appl. Mater. Interfaces. **7**, 8757–8769 (2015)
81. M.T. Shabbir, T. Hussain, S. Shakir, M. Anwar, A.H. Khoja, S. Nawaz, A.N. Satti, Enhancement in the photocatalytic and optoelectronic properties of erbium oxide by adding zinc oxide and molybdenum. Ceram. Int. **49**, 19691–19700 (2023)
82. A. Brik, S. Naama, T. Hadjersi, M.E.A. Benamar, S. Bouanik, A. Manseri, Photodegradation of methylene blue under UV and visible light irradiation by Er_2O_3-coated silicon nanowires as photocatalyst, Reaction Kinetics, Mechanisms and Catalysis, 131 (2020) 525–536
83. T. Munawar, F. Mukhtar, M.S. Nadeem, K. Mahmood, M. Hasan, A. Hussain, A. Ali, M.I. Arshad, F. Iqbal, Novel direct dual-Z-scheme ZnO-Er2O3-Nd2O3@reduced graphene oxide heterostructured nanocomposite: synthesis, characterization and superior antibacterial and photocatalytic activity. Mater. Chem. Phys. **253**, 123249 (2020)
84. P.T. Thu, V.D. Thinh, V.D. Lam, T.N. Bach, L.T.H. Phong, D.H. Tung, D.H. Manh, N. Van Khien, T.X. Anh, N.T.H. Le, Decorating of Ag and CuO on ZnO Nanowires by Plasma Electrolyte Oxidation Method for Enhanced Photocatalytic Efficiency, Catalysts, 12 (2022) 801
85. K. Xu, J. Wu, C.F. Tan, G.W. Ho, A. Wei, M. Hong, Ag–CuO–ZnO metal–semiconductor multiconcentric nanotubes for achieving superior and perdurable photodegradation. Nanoscale. **9**, 11574–11583 (2017)
86. E.T. Debele, T.D. Desissa, O.A. Zelekew, F.F. Bakare, G.B. Feyisa, T.H. Wondimu, Plant-Mediated Synthesis of Ni-Doped CuO and Fe_2O_3 Nanocomposite for Photodegradation of Methylene Blue Dye, Journal of Nanomaterials, 2023 (2023) 3678679
87. H. Katsumata, Y. Oda, S. Kaneco, T. Suzuki, Photocatalytic activity of Ag/CuO/WO_3 under visible-light irradiation. RSC Adv. **3**, 5028–5035 (2013)